Linking simple molecules to grain evolution across planet-forming disks

Salinas Poblete, V.N.

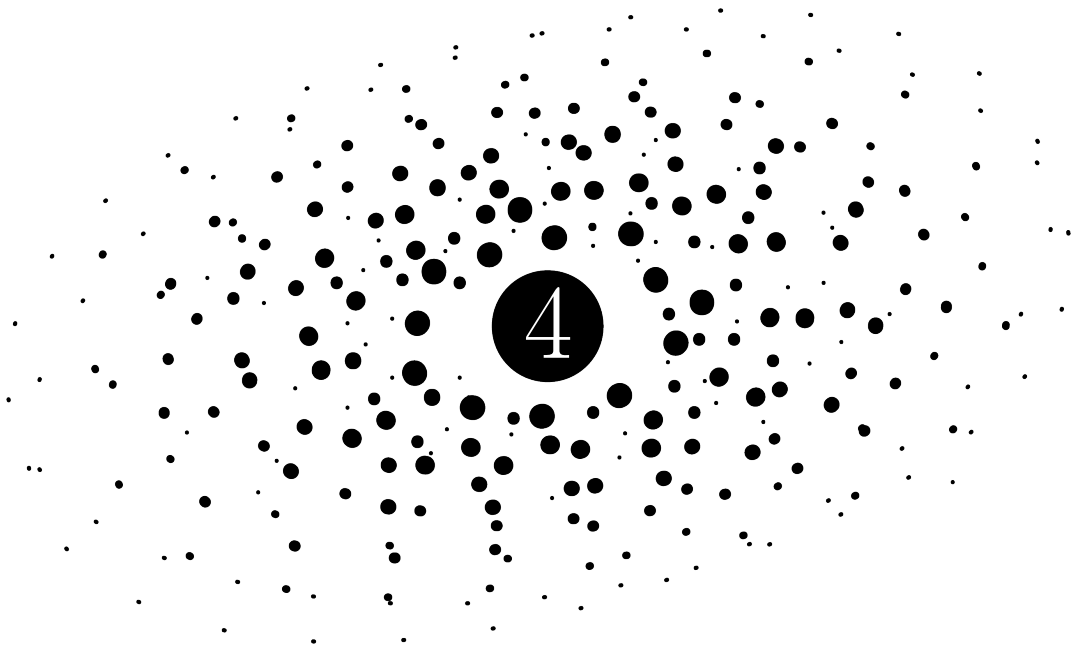

4

Comparing detections and upper limits of NH_3 and NH_2D in the disks of TW Hya and HD163296

Salinas, V. N., Hogerheijde, M. R., Kama, M. in prep.

4.1 Introduction

Nitrogen within Solar System bodies, inherited from the Solar Nebula, takes a variety of forms: N_2 on Earth, organics in meteorites, and NH_3 and organics in comets (Schwarz & Bergin 2014; Mumma & Charnley 2011). Most bodies are furthermore strongly depleted in nitrogen, compared to oxygen and carbon (Pontoppidan et al. 2014). In the interstellar medium 10%-20% of nitrogen is contained in ices such as NH_3, NH_4^+, and XCN, the latter of which is mostly in the form of OCN^- (Öberg et al. 2011). The remainder of the nitrogen budget is thought to reside in the gas in atomic and molecular form, and does not represent a suitable reservoir to deliver nitrogen to rocky planets, meteorites, and comets. Molecular and atomic nitrogen is not directly observable in the dense interstellar medium (ISM). However, most of the simple nitrogen-bearing ices have been detected in the gas-phase toward star forming regions. Their initial abundances are critical for the understanding of the chemical composition of nitrogen-bearing species throughout the star formation process and, consequently, Solar System bodies.

Ammonia is one of the main ice reservoirs of nitrogen and is readily detected in star forming regions (Bottinelli et al. 2010; Daranlot et al. 2012; Boogert et al. 2015). It has only been recently detected, for the first time, toward the old planet-forming disk around TW Hya using *Herschel*/HIFI by Salinas et al. (2016). Our modelling, that considered different radial distributions of ammonia high in the upper layers of the disk as well as settled and compact models, showed that the total vapor mass estimates can range across two orders of magnitude. Only the most settled and compact model (Cm), following the same distribution of mm-size grains (Andrews et al. 2012), is in agreement with the expected NH_3/H_2O ratio and ortho to para ratio (OPR) of water in comets. Detailed chemical models have shown ammonia to be able to form as a product of several processes at large radii, namely warm gas-phase chemistry, ion-molecule chemistry and photodesorption processes (Walsh et al. 2015). On grains, ammonia forms through atomic nitrogen hydrogenation (Brown & Millar 1989; Hiraoka et al. 1995; Hidaka et al. 2011; Fedoseev et al. 2015). Processes to release NH_3 from ice to gas at temperatures below the thermal desorption include cosmic-ray desorption (Hasegawa & Herbst 1993), reactive desorption (Garrod et al. 2007) and photodesorption (Prasad & Tarafdar 1983; Hartquist & Williams 1990). The formation of ammonia in grains dominates in the very early stages of star formation. In more evolved stages, where protoplanetary disks are formed, the dominant process shifts to gas-phase formation (Sipilä et al. 2015; Harju et al. 2017). This process occurs through a well-known chain of reactions, starting with the dissociation of N_2 (by photo-processes or He^+) and terminating in $NH_4^+ + e \rightarrow NH_3 + H$ (Le Gal et al. 2014; Roueff et al. 2015; Walsh et al. 2015).

Observations of gas-phase ammonia in cold star-forming cores (Daniel et al. 2016; Pillai et al. 2011; Busquet et al. 2010; Crapsi et al. 2007; Roueff et al. 2005) and ices in comets (Crovisier et al. 2004) show very high NH_2D/NH_3 ratios of ~0.5 and ~0.05 respectively [1]. This high NH_2D/NH_3 ratio suggests formation on cold environments. However, the deuteration of ammonia in the gas-phase is dominated by the isotopologues of H_3^+ and is faster and more efficient than deuteration on grains (Harju et al. 2017; Sipilä et al. 2015). TW Hya and HD163296 are known to harbor deuterated species, like DCN with deuterium fractionations of 0.017 and 0.016 respectively (Öberg et al. 2012; Huang et al. 2017), DCO^+ with deuterium fractionations of 0.035 and 0.048 respectively (van Dishoeck et al. 2003; Huang et al. 2017) and N_2H^+ with a deuterium fractionation of ~0.4 toward HD163296 (Salinas et al. 2017). In prestellar cores, NH_2D/NH_3 is found to be consistently higher than

[1] The NH_2D/NH_3 ratio is different than the atomic D/H ratio of NH_3, which accounts for the number of H atoms in NH_3.

DCO^+/HCO^+ and DCN/HCN (Treviño-Morales et al. 2014). Together, this suggest that disks around HD163296 and TW Hya may be equally rich in NH_2D.

We first aim to constrain the amount of gas-phase NH_3 in HD 163296, in comparison to TW Hya. Secondly, we observed o-NH_2D towards HD 163296. Since we do not observe the same line in TW Hya, we assume that the NH_2D/NH_3 ratio in the gas-phase is 0.1 and compare the expected NH_2D mass with the upper limits derived for HD 163296. Finally, we estimate the integration time in ALMA to detect the NH_2D line in HD 163296 and TW Hya. Section 4.2 presents the data and their reduction. Section 4.3 contains our modeling approach and Section 4.4 the resulting upper limits on the NH_3 and NH_2D vapor masses. Section 4.5 discusses the implication of our models and compares the values obtained for HD163296 to those of TW Hya. We also predict line fluxes for deuterated ammonia toward TW Hya. Finally, Section 4.6 summarizes our conclusions.

4.2 Observations

Observations of o-NH_3 $1_0 - 0_0$ in TW Hya ($\alpha_{2000} = 11^h01^m51\overset{s}{.}91$, $\delta_{2000} = -34°42'17\overset{''}{.}0$) were previously presented by Salinas et al. (2016) and were obtained using the Heterodyne Instrument for the Far-Infrared (HIFI) as part of the key program 'Water in Star-Forming Regions with *Herschel*' (WISH) (van Dishoeck et al. 2011). We now present observations toward the Herbig Ae star HD 163296 ($\alpha_{2000} = 17^h56^m51\overset{s}{.}21$, $\delta_{2000} = -21°57'22\overset{''}{.}0$) as part of the same program taken on 2010 March 21 of the o-NH_3 $1_0 - 0_0$ line at 572.49817 GHz using receiver band 1b and a local oscillator tuning of 551.895 GHz (OBS-ID 1342192516). With a total on-source integration of about 20 min, the observation was taken with system temperatures of 75-95 K. The data were recorded in the Wide-Band Spectrometer (WBS) which covers 4.4 GHz with 1.1 MHz resolution. This corresponds to 0.59 km s^{-1} at 572 GHz. A beam efficiency $\eta_{nb} = 0.64$ was used to calibrate the data and the procedure is identical to that of Du et al. (2017).

We also present ALMA Band 8 archival observations of the p-NH_2D $1_0 - 0_0$ line at 494.454 GHz toward HD 163296 (project 2013.1.00527.S) taken on 2015 May 2. The total integration time on source was 14 min with thirty-six 12 m antennas. The system temperature varied from 500 to 900 K. The correlator set up had 4 different spectral windows (SPW). Two of these SPW contain the [CI] atomic line at 492.160 GHz and the p-NH_2D $1_0 - 0_0$ line at 494.454 GHz with spectral resolutions of 488 kHz (0.30 km s^{-1}) and 244 kHz (0.15 km s^{-1}) respectively. The other two SPW contain wideband (2 GHz) continuum centered at 480.236 GHz and 482.047 GHz. The quasars J1256-0547 and J1733-1304 were used as bandpass and gain calibrators respectively. Titan was used as total flux calibrator using the Butler-JPL-Horizons 2012 flux models for Solar System objects available through the Common Astronomy Software Applications (CASA). The data were calibrated following the standard CASA reduction as provided in the calibration scripts by ALMA. Baselines in the antenna array configuration correspond to a range in *uv*-distance of 30–570 kλ, which translates into a beam of $\sim 0\overset{''}{.}36$. Self-calibration was applied to the data using the continuum emission from the two SPW containing wideband continuum and the line-free channels of the SPW containing high-spectral resolution data. We used DV02 as a reference antenna. We calculated calibration solutions twice for phase, first using a solution interval of 125 s and secondly together with amplitude using a solution interval if 6.05 s corresponding to the integration scan. A minimum of 4 antennas and a signal-to-noise (S/N) of 2 was required for the solution to be valid. The data were continuum subtracted in the *uv*-space using a zero-order polynomial fit and imaged using the CLEAN task in CASA with natural weighting.

The p-NH_2D $1_0 - 0_0$ and o-NH_3 $1_0 - 0_0$ observations resulted in non-detections for these modest integration times. The channel maps in the spectral cube of the p-NH_2D $1_0 - 0_0$ reached a sensitivity of 30 mJy beam^{-1} channel^{-1}. In Table 4.1 we report upper limits for these transitions and the total line flux of the o-NH_3 $1_0 - 0_0$ transition toward TW Hya. Figure 4.1 shows the calibrated spectra of HD163296 and TW Hya for the selected lines.

4.3 Modeling Approach

In this section we describe our adopted physical models and two different parametrizations of the abundance of ammonia and its deuterated isotope. We assume that deuterated ammonia follows the same distribution as its non-deuterated isotope to translate the derived total line flux upper limits into total masses. Although this assumption is not necessarily true if their formation pathways are different, it translates as a lower limit on the NH_2D/NH_3 ratio because gas-phase NH_2D might not be present in the regions where gas-phase NH_3 exists. By comparing the amounts of ammonia of the two disks we aim to make a prediction for upcoming observations of the expected line flux of deuterated ammonia for both disks.

4.3.1 Physical structure

We model the physical structure of both disks with models found previously in the literature. We adopt the physical models of Cleeves et al. (2015) for TW Hya and of Mathews et al. (2013) for HD163296. Cleeves et al. (2015) used HD measurements (Bergin et al. 2013) to constrain a total gas mass for the disk of TW Hya of 0.04 ± 0.02 $M_\odot$ whereas Mathews et al. (2013) fitted the SED of HD 163296 and used a dust to gas ratio of 0.0065 (Draine & Lee 1984). The dust surface density profile is defined by the following expression

$$\Sigma_d(R) = \begin{cases} \Sigma_c \left(\frac{R}{R_c}\right)^{\gamma} \exp\left[-\left(\frac{R}{R_c}\right)^{(2-\gamma)}\right] & \text{if } R_{in} \leq R \leq R_{out} \\ 0 & \text{if } R < R_{in} \text{ or } R > R_{out} \end{cases} \tag{4.1}$$

and their vertical distribution by a scale height of the form

$$H(R) = H_c \left(\frac{R}{R_c}\right)^{\psi}, \tag{4.2}$$

where R_c is a characteristic radius, γ represents the radial dependency of the disk viscosity, ψ describes the power law disk flaring, and R_{in} and R_{out} the inner and outer radii of the disk. The H_c takes four different values for the HD163296 model: H_{small} and H_{large} to describe the small and large population of dust grains, and H_{main} and H_{tail} that describe the gas distribution as two-component model with a term f_{tail} describing the fraction of the total gas mass in the tail component. The adopted TW Hya model makes no distinction between large and small dust populations (see Appendix A.2 of Cleeves et al. 2015). Both models do not consider a radial separation of small and large dust grain populations. Table 4.2 shows the adopted values of the parameters described above for both sources.

We also adopt their estimated gas temperature profile $T(R, z)$ calculated from the ultraviolet radiation field throughout the disk by using the radiative transfer code TORUS in the case of TW Hya (see Appendix A of Cleeves et al. 2015, and references therein) and the axisymmetric 3D radiative transfer code RADMC in the case of HD163296 (Dullemond & Dominik 2004).

Table 4.1: Observed line parameters.

Source	Transition	$F_{\rm line}$ (10^{-19} W m^{-2})^{a,b}	$V_{\rm LSR}$ (km s^{-1})^{b}	FWHM (km s^{-1})^{b}	$T_{\rm mb}$ (mK km s^{-1})
TW Hya	o-NH_3 $1_0 - 0_0$	1.1±0.13	3.0±0.06	0.9±0.06	15.1±2.1
HD163296	o-NH_3 $1_0 - 0_0$	<2.1	5.8	9.0	<36.9
HD163296	p-NH_2D $1_0 - 0_0$	<0.3	5.8	9.0	<8.8^{c}

Notes. $^{(a)}$ The upper limit for p-NH_2D $1_0 - 0_0$ is equal to 3σ, where σ is the rms of the spectra from a square box of 10.″0 × 10.″0. The errors and upper limits are calculated taking the random errors due to noise only and do not include the calibration uncertainty, estimated to be about 20% of the total flux in the case of observations taken with *Herschel*. $F_{\rm line}$ is the integrated flux from $V_{\rm LSR}$= +1.5 to +4.1 km s^{-1} in the case of TW Hya, and from $V_{\rm LSR}$= +1.3 to +10.3 km s^{-1}. $^{(b)}$ For TW Hya these are the results of a Gaussian fit, for HD163296 the values of $V_{\rm LSR}$ and FWHM are taken from Mathews et al. (2013). Errors on $V_{\rm LSR}$ and FWHM are formal fitting errors and much smaller than the spectral resolution of 0.26 km s^{-1}. $^{(c)}$ This integrated line flux was calculated diluting the ALMA signal to the correspondent *Herschel* beam of 44.″0 at the observed frequency of 493.454 GHz assuming a source size of 10.″0 × 10.″0.

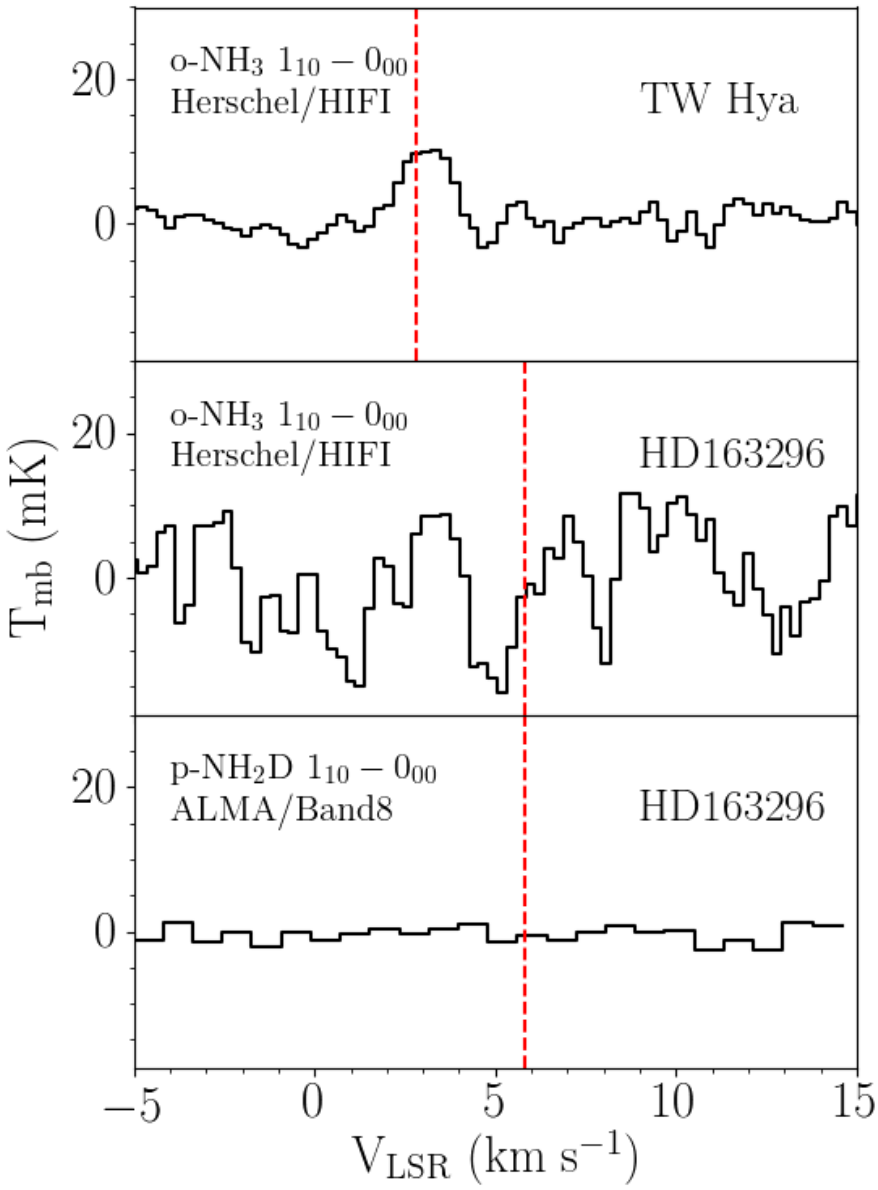

Figure 4.1: Observed spectra of o-NH_3 $1_0 - 0_0$ with *Herschel* toward TW Hya and HD163296 and of p-NH_2D $1_0 - 0_0$ with ALMA Band 8 toward HD163296. The ALMA signal was beam diluted to the correspondent *Herschel* beam of 44.″0 at 493.454 GHz.

Table 4.2: Adopted model parameters.

Disk parameters	HD163296	TW Hya
Σ_c	0.037 g cm^{-2}	0.040 g cm^{-2}
R_c	150 AU	150 AU
R_{in}	0.6 AU	4.0 AU
R_{out}	540 AU	200 AU
γ	1.0	1.0
ψ	0.066	0.3
H_{small}	12 AU	15 AU
H_{large}	9 AU	3 AU
H_{main}	15 AU	15 AU
H_{tail}	30 AU	–
f_{tail}	0.016	–

4.3.2 Parametric abundance models

We consider two different abundance models for ammonia and its single deuterated isotopologues in both disks. The first model simply consists of an extended and constant (model Ec) abundance throughout the entire disk. The second model considers that, in both disks, we expect the distribution of the mm-size grains to have settled to the midplane and migrated inwards as supported by observations of the continuum emission (Andrews et al. 2016; Zhang et al. 2016). Figure 4.2 shows a diagram of these two models. They are analogues of the Cm and Em models of TW Hya presented in (Salinas et al. 2016). In TW Hya, ammonia (and water) is thought to be released to the gas-phase from its icy reservoir, possibly locked in large planetesimals bodies, that follow the distribution of mm-size dust grains (Salinas et al. 2017). Thus we set the Cm model as our preferred model. We implement this settled and compact distribution (Cm) of ammonia and its single deuterated isotope as a constant abundance with respect to $n(H_2)$ following the mm-size dust grain distribution of Andrews et al. (2012) with H_c= 10.31, ψ=1.25 and R_c= 100 AU at R <60 AU for TW Hya and with H_c= 9.0 AU, ψ=0.066 and R_c at R <290 AU for HD163296 (Mathews et al. 2013; Zhang et al. 2016).

4.3.3 Line excitation and radiative transfer

We used LIME (v1.5), a non-LTE 3D radiative transfer code (Brinch & Hogerheijde 2010) that can predict line and continuum radiation from a source model. All of our models use 50000 grid points. Grid points are distributed randomly in R using a logarithmic scale. This means in practice that inner regions of the disk have a finer sampling than the outer parts of the disk. We perform our calculation in LTE since non-LTE calculations of representative models are indistinguishable from their LTE counterparts. This is due to the relatively low critical density, of only a few 10^7 cm^{-3} for transitions, compared to the densities at the midplane of the adopted models of TW Hya and HD163296. The rate coefficients for o-NH_3 and p-NH_2D were taken from the Leiden Atomic and Molecular Database (Schöier et al. 2005; Daniel et al. 2014; Danby et al. 1988)[2].

[2] www.strw.leidenuniv.nl/~moldata/

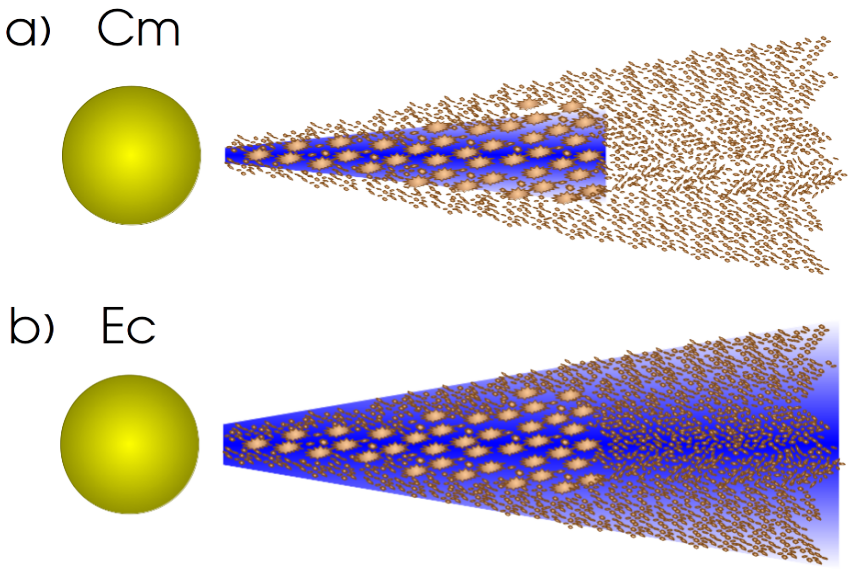

Figure 4.2: Diagram of the compact and settled (Cm), and the extended and constant (Ec) distribution of ammonia. The blue region highlights the location of ammonia following the mm-size grains (Cm) and the entire disk (Ec).

Table 4.3: Upper limits on total vapor masses in the HD163296 disk.

Species	Cm	Ec
o-NH_3	$< 8.5 \times 10^{20}$ g	$< 1.4 \times 10^{21}$ g
p-NH_2D	$< 1.5 \times 10^{20}$ g	$< 6.5 \times 10^{20}$ g

Forty channels of 0.4 km s^{-1} and 0.1 km s^{-1} each, for HD163296 and TW Hya models respectively, were used for all line models with 200 pixels of 0.05 arcsec. Because we aimed at comparing these models with spatially unresolved data, we calculated the total flux by summing all the pixels after subtracting the continuum.

4.4 Results

Figure 4.3 shows the resulting line flux for the targeted lines in the *Herschel* beam as a function of o-NH_3 and p-NH_2D total vapor masses. The slope of the curves are consistent with increasing opacity going from an optically thin regime (flux (F) $\propto$ column density(N)) to saturated ($F \propto \sqrt{\ln(N)}$) as the wings of the line become gradually optically thick.

In the optically thin regime (low total vapor masses) the Cm models result in higher line fluxes than in the Ec models for an equal total vapor mass. At lower vapor masses our radially compact (Cm) model lies within higher temperatures than a radially extended (Ec) model resulting in the observed behavior. In the asymptotic regimes (high total vapor masses), the compact Cm models result in less total flux than the larger Ec models. At higher vapor masses the lines become fully thick and trace only a very thin region at the disk surface, hence the Cm model yields less flux than the Ec because of its smaller emitting size.

Table 4.3 summarizes the upper limits on the total vapor mass of o-NH_3 and p-NH_2D in HD163296 obtained by the intersection of the total line flux for our two models, as shown in Fig. 4.3, with the upper limits on the total line fluxes listed in Table 4.1. These total line flux 3σ upper limits of o-NH_3 1_0–0_0 and p-NH_2D 1_0–0_0 correspond to total vapor masses of 0.9-1.4$\times10^{21}$ g and 1.5-6.5$\times10^{20}$ g, equivalent to disk-averaged abundances of 0.8-2.7$\times10^{-11}$ and 4.0-5.0$\times10^{-12}$, respectively. The estimates on the total vapor mass of o-NH_3 include the statistical error on the observations and the systematic errors on the total line flux, estimated to be about 20%.

4.5 Discussion

4.5.1 Total gass masses and deuteration estimates

The upper limit on the o-NH_3 total vapor mass in HD163296 is a factor of 5-10 higher than the upper limit on the p-NH_2D total vapor mass. The upper limit on the o-NH_3 total vapor mass in HD163296 of 0.9-1.4$\times10^{21}$ g is a factor 10 lower than the o-NH_3 total vapor mass detected in TW Hya (1.1$\times10^{22}$ g) by Salinas et al. (2016) adopting their preferred Cm model. Since the adopted disk mass of HD163296 is twice that of TW Hya, this leads us to conclude that the HD163296 disk is relatively poorer in NH_3.

The dashed vertical lines in Fig. 4.3 show different estimates of the total amount of vapor mass of o-NH_3 that could be present in HD163296. The first estimate of ~2.2$\times10^{22}$ g ($E_{TW\ Hya}$) corresponds to twice the o-NH_3 total vapor mass (1.1$\times10^{22}$ g) detected in TW

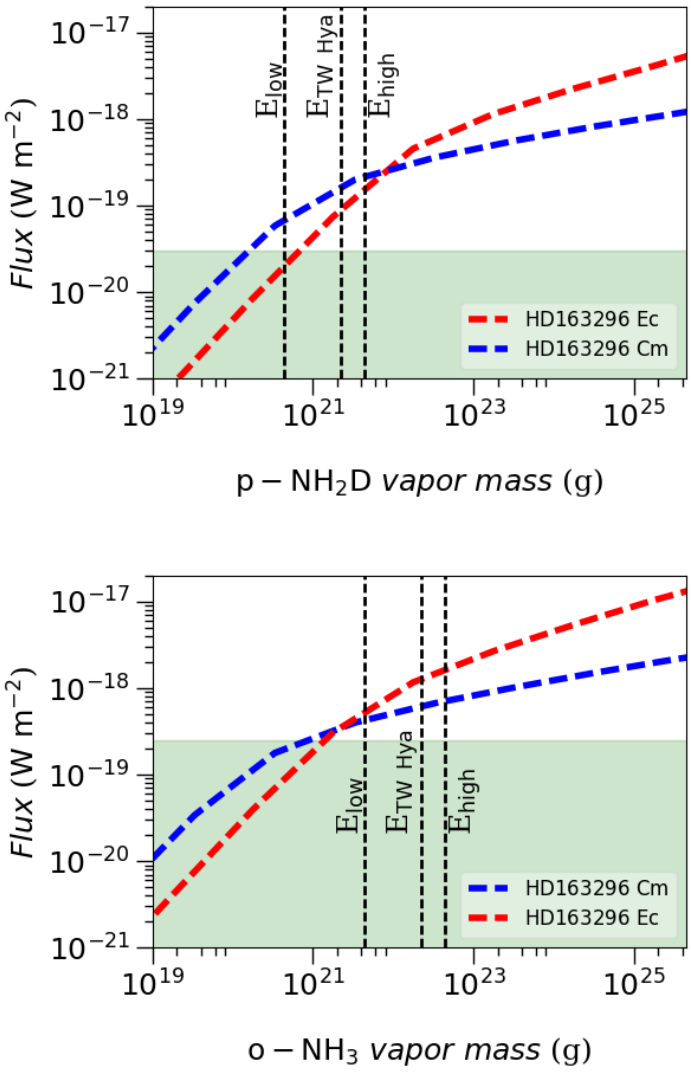

Figure 4.3: Resulting total line flux of our Cm and Ec models toward HD163296 for p-NH_2D 1_0–0_0 and o-NH_3 1_0–0_0 as a function of total vapor mass. The green area shows the derived total line flux 3σ upper limits of $< 0.3 \times 10^{-19}$ Wm^{-2} and $< 2.1 \times 10^{-19}$ Wm^{-2} for the p-NH_2D 1_0–0_0 and o-NH_3 1_0–0_0 lines, respectively. The dashed vertical lines show estimates for the vapor mass obtained by assuming that the amounts of o-NH_3 toward TW Hya and HD163296 are comparable (see Sec. 4.5.1). The estimates for p-NH_2D are scaled down versions of the o-NH_3 estimates assuming a deuterium fractionation of 10% and an OPR of ammonia of unity.

Hya since the adopted total mass of HD163296 is twice that of TW Hya. The second (E_{High}) and third (E_{Low}) estimates, of ~4.4×10^{22} g and of ~4.4×10^{21} g respectively, are calculated scaling the first E_{TWHya} estimate by factors of 2 and 0.2. These factors account for the relative amounts of other nitrogen-bearing species, namely HCN (factor of 2) and N_2H^+ (factor of 0.2), of HD163296 with respect to TW Hya. The HCN mass in TW Hya is only half that of HD163296, while the N_2H^+ in TW Hya is 5 times larger than in HD163296. The amount of HCN is calculated by scaling the $H^{13}CN$ data of HD163296 by an adopted $^{12}C/^{13}C$ ratio of 69 (Huang et al. 2017). We therefore conclude that, for the assumed disk masses, the low o-NH_3 amount in HD163296 in comparison to that of TW Hya is due to chemical differences and not to the overall content of elemental nitrogen in these disks. If we consider desorption from ices to be the dominant mechanism to release NH_3 into the gas-phase, environmental conditions in TW Hya, such as a high X-ray radiation field or a local decrease in UV opacity, can enhance the production of gas-phase NH_3 in comparison to HD163296. In the gas-phase, formation of ammonia could also be enhanced by a higher X-ray/UV radiation field, since the chemical pathway to produce NH_3 starts by the dissociation of molecular nitrogen by either photo-processes or He^+.

Alternatively, this difference can also be reconciled by considering a lower mass of the disk around HD163296. The work by Kama et al. (2015) suggest a lower gas-to-dust ratio for the inner disk around HD163296 as an explanation for the decreased photospheric abundance of refractory elements. They report a gas-to-dust ratio a factor of 2-4 lower than the value of our adopted model. The corrected estimates of o-NH_3 in HD163296, considering these lower gas-to-dust ratios, would be a factor of 2-4 lower than the ones presented above and consistent with our non-detections at levels similar to those of TW Hya.

The upper limit on the p-NH_2D total vapor mass in HD163296 of 1.5-6.5$\times10^{20}$ g is a factor 5-10 lower than the p-NH_2D total vapor mass estimate in TW Hya of 1.1×10^{21} g. This estimate is calculated from the inferred o-NH_3 considering the Cm model of Salinas et al. (2016) and assuming a deuterium fractionation of 10%, equal to the canonical value in protostellar dense cores (Roueff et al. 2005; Busquet et al. 2010), together with an OPR of NH_2D of unity. The top panel of Figure 4.3 shows limits on the p-NH_2D total vapor masses in HD163296. These are calculated by scaling down the previous estimates on the o-NH_3 total vapor masses in the same disk by a factor of 0.1 accounting for a deuterium fractionation of 10%.

The non-detection of the p-NH_2D $1_0 - 0_0$ line at the modest integration times here presented does not add any new information on the amount of ammonia in HD163296, but is consistent with a lower amount of ammonia in this disk in comparison with TW Hya. However, other effects can be responsible for the non-detection of the p-NH_2D $1_0 - 0_0$ line toward HD163296 such as a much lower deuterium fractionation or a lower OPR of ammonia. The expected OPR of ammonia at low spin temperatures is ~3 (Daniel et al. 2016) in contrast to the high temperature limit of unity at $T_{spin} > 30$ K. If p-NH_2D is being released near the midplane into the gas-phase from the grains together with o-NH_3 this low value of the upper limit could reflect its formation pathway.

4.5.2 ALMA predictions

Both our compact and extended radial distributions are consistent, at low vapor masses, with the obtained o-NH_3 and p-NH_2D total line flux upper limits. Nevertheless, our models predict the same total line flux for different total vapor masses depending on their radial distribution. ALMA can provide the spatial resolution needed to distinguish the radial location of NH_2D and, indirectly, of NH_3. In addition, ALMA is also more sensitive than

Herschel (Fig. 4.1). From Fig. 4.3 our Ec model of p-NH_2D $1_0 - 0_0$ line in HD163296 results in 1.9×10^{-20} W m^{-2} for a deuteration fractionation of 0.1 and the lowest o-NH_3 total vapor mass estimate of 4.4×10^{20} gr. We can detect a 5σ signal of the total integrated flux with ALMA [3] of our Ec model in $\sim$ 20 min. This calculation was made using 43 antennas and a water vapor column density of 0.66 mm corresponding to a T_{sys} of 615 K. We also assume a bandwidth equivalent to the adopted FWHM (see Table 4.1) of the line of 9 km s^{-1}. A total integrated flux detection would constrain the total amount of p-NH_2D but a spatially resolved detection in individual channels is needed to constrain the radial and vertical distribution of p-NH_2D.

Although we did not observed TW Hya, it is two times closer than HD163296 and, as stated above, has at least 5 times more o-NH_3. The expected total flux of this line is shown in Fig. 4.4 as a function of total vapor mass. We have an accepted ALMA Cycle 4 proposal that has received rank A to observe the o-NH_2D 1_0–0_0. We target this line, instead of the p-NH_2D 1_0–0_0 line, advocating for the expected higher OPR ratio of 3 for ammonia and deuterated ammonia at low temperatures (Sipilä et al. 2015) as argued above. Figure 4.5 shows simulated ALMA observations of the two radially compact models, Cm and Cp, described in Salinas et al. (2016, see Chapter 3) with 2.5 h of integration time using a deuterium fractionation of 5%. The Cm model places gas-phase ammonia in the midplane, the same way as presented in this work, while the Cp model places gas-phase ammonia in the upper photodominated layers of the disk. These radially compact models are brighter than the radially extended ones for their best-fit vapor masses. At this resolution (42 au at the source distance of 56 pc) and the proposed sensitivity, we expect to detect line emission for all four radial and vertical distributions considered by Salinas et al. (2016) if the deuteration ratio NH_2D/NH_3 is high (0.5), and to detect only the two radially compact models (<60 AU) down to a deuterium fractionation for ammonia as low as 5%. Thus, our proposed observations allow us to directly test our hypothesis that NH_2D, and by inference NH_3, is co-located with the millimeter-sized grains at radii <60 AU, for deuterium fractionation values comparable to prestellar cores.

4.6 Summary & Conclusions

We have modeled the o-NH_3 1_0–0_0 and p-NH_2D 1_0–0_0 lines toward HD163296 considering two different models: a compact and settled configuration following the mm-size grains and an extended configuration following the full extent of the gas. We have derived upper limits on the total amount of o-NH_3 and p-NH_2D vapor mass (and disk-averaged abundances) from these models of 0.8-1.4$\times10^{21}$ g (0.8-2.7$\times10^{-11}$) and 1.5-6.5$\times10^{20}$ g (4.0-5.0$\times10^{-12}$) respectively, and contrasted them with the amount of nitrogen-bearing species detected in TW Hya.

We conclude that the non-detections of the o-NH_3 1_0–0_0 and p-NH_2D 1_0–0_0 lines toward HD163296 suggest that this disk is NH_3 poor compared to the similar-mass disk of TW Hya for the adopted models. We argue that this difference is due to its chemical origin by also comparing with other nitrogen-bearing species reported in the literature toward these two sources. Full chemical modeling of these species and spatially resolved observations of these disks are needed to disentangle the different distributions and formation pathways of NH_3 and NH_2D.

[3] Calculations performed with the ALMA sensitivity calculator https://almascience.eso.org/proposing/sensitivity-calculator

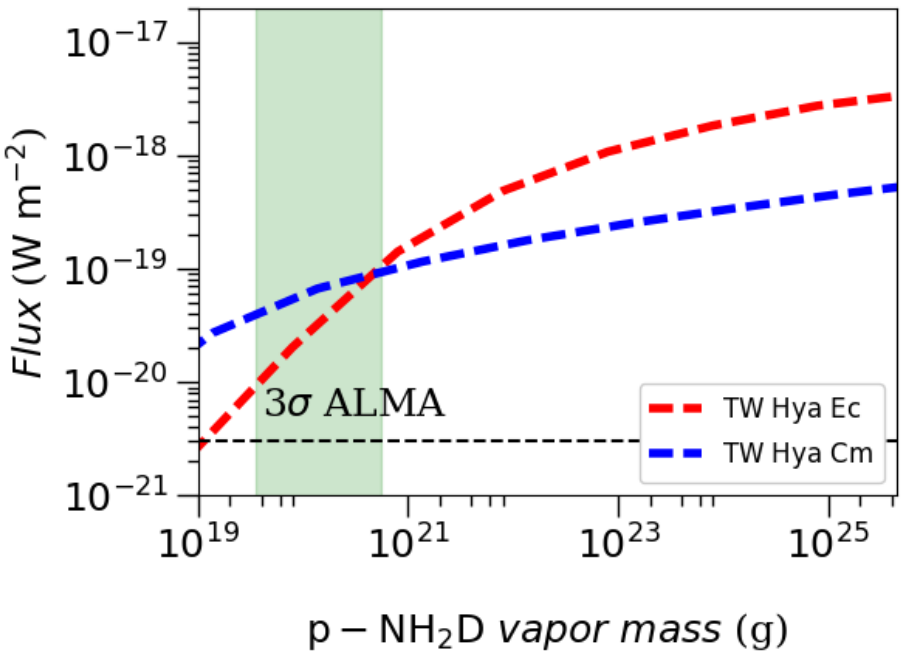

Figure 4.4: Resulting total line flux of our Cm and Ec models toward TW Hya for p-NH_2D $1_0 - 0_0$ as a function of total vapor mass. The colored region show the expected range of vapor masses taken from the different models of Salinas et al. (2016) assuming a 5% deuterium fractionation and an OPR of unity. The dashed line shows the 3σ ALMA detection limit for an integrated line flux over a bandwidth of 1 km s^{-1} in 2.5 h.

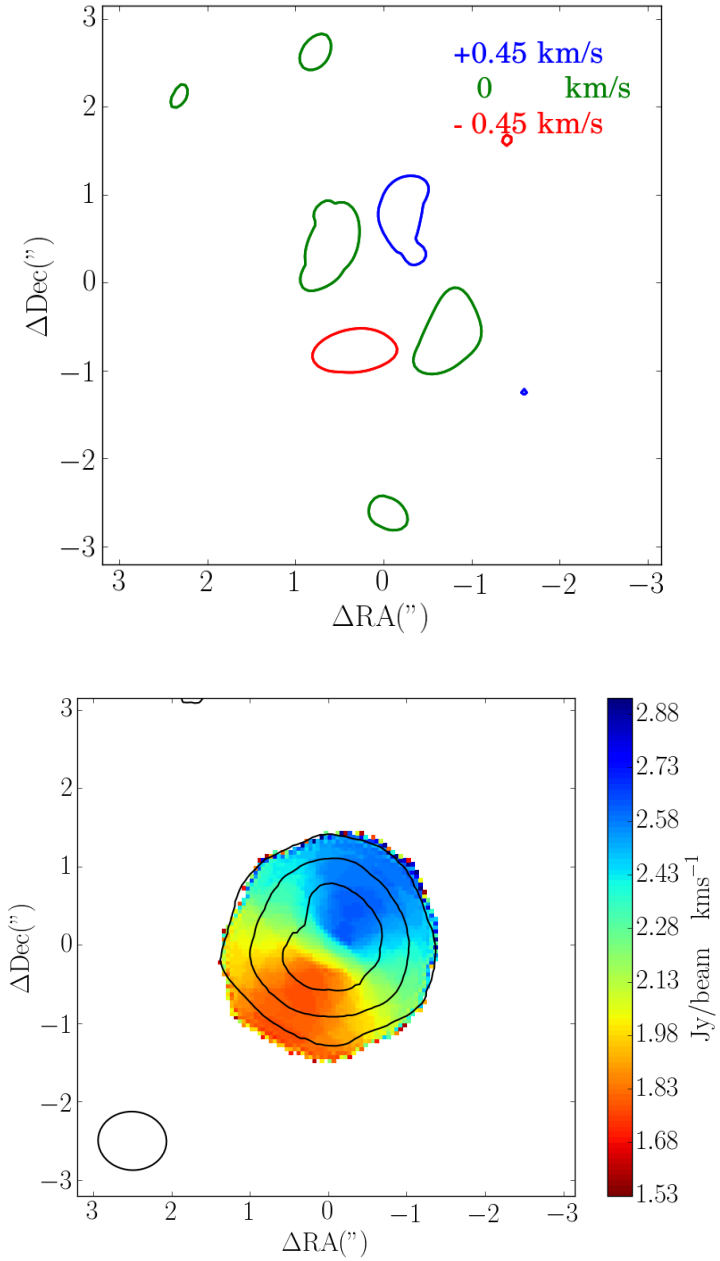

Figure 4.5: Simulated ALMA images of the expected o-NH_2D $1_0 - -0_0$ emission for a low NH_2D/NH_3 ratio of 0.05 and an assumed radial distribution for ammonia <60 AU. The right panel shows the velocity-centroid (color) and integrated intensity (contours of 5, 10 and 15 σ-levels) of a model with all ammonia residing near the disk midplane; the left panel shows the detection limit of our proposed observations, corresponding to a model with all ammonia residing at radii <60 AU but at large heights in the disk (3-σ contours at 3 different velocities).

Acknowledgements. This work was partially supported by grants from the Netherlands Organization for Scientific Research (NWO) and the Netherlands Research School for Astronomy (NOVA) This paper makes use of the following ALMA data: ADS/JAO.ALMA# 2013.1.01268.S. ALMA is a partnership of ESO (representing its member states), NSF (USA), and NINS (Japan), together with NRC (Canada), NSC and ASIAA (Taiwan), and KASI (Republic of Korea), in cooperation with the Republic of Chile. The Joint ALMA Observatory is operated by ESO, AUI/NRAO, and NAOJ. *Herschel* is a European Space Agency space observatory with science instruments provided by European-led principal investigator consortia and with important participation from NASA. HIFI has been designed and built by a consortium of institutes and university departments from across Europe, Canada, and the United States under the leadership of SRON Netherlands Institute for Space Research, Groningen, The Netherlands, and with major contributions from Germany, France, and the US. Consortium members are: Canada: CSA, U. Waterloo; France: IRAP (formerly CESR), LAB, LERMA, IRAM; Germany: KOSMA, MPIfR, MPS; Ireland, NUI Maynooth; Italy: ASI, IFSI-INAF, Osservatorio Astrofisico di Arcetri-INAF; Netherlands: SRON, TUD; Poland: CAMK, CBK; Spain: Observatorio Astronómico Nacional (IGN), Centro de Astrobiología (CSIC-INTA). Sweden: Chalmers University of Technology – MC2, RSS & GARD; Onsala Space Observatory; Swedish National Space Board, Stockholm University – Stockholm Observatory; Switzerland: ETH Zurich, FHNW; USA: Caltech, JPL, NHS. Support for this work was provided by NASA (*Herschel* OT funding) through an award issued by JPL/Caltech. The data presented here are archived at the *Herschel* Science Archive, http://archives.esac.esa.int/hda/ui, under OBSID 1342198337 and 1342201585.

Bibliography

Andrews, S. M., Wilner, D. J., Hughes, A. M., et al. 2012, ApJ, 744, 162
Andrews, S. M., Wilner, D. J., Zhu, Z., et al. 2016, ApJ, 820, L40
Bergin, E. A., Cleeves, L. I., Gorti, U., et al. 2013, Nature, 493, 644
Boogert, A. C. A., Gerakines, P. A., & Whittet, D. C. B. 2015, ARA&A, 53, 541
Bottinelli, S., Boogert, A. C. A., Bouwman, J., et al. 2010, ApJ, 718, 1100
Brinch, C., & Hogerheijde, M. R. 2010, A&A, 523, A25
Brown, P. D., & Millar, T. J. 1989, MNRAS, 240, 25P
Busquet, G., Palau, A., Estalella, R., et al. 2010, A&A, 517, L6
Cleeves, L. I., Bergin, E. A., Qi, C., Adams, F. C., & Öberg, K. I. 2015, ApJ, 799, 204
Crapsi, A., Caselli, P., Walmsley, M. C., & Tafalla, M. 2007, A&A, 470, 221
Crovisier, J., Bockelée-Morvan, D., Colom, P., et al. 2004, A&A, 418, 1141
Danby, G., Flower, D. R., Valiron, P., Schilke, P., & Walmsley, C. M. 1988, MNRAS, 235, 229
Daniel, F., Faure, A., Wiesenfeld, L., et al. 2014, MNRAS, 444, 2544
Daniel, F., Coudert, L. H., Punanova, A., et al. 2016, A&A, 586, L4
Daranlot, J., Hincelin, U., Bergeat, A., et al. 2012, Proceedings of the National Academy of Science, 109, 10233
Draine, B. T., & Lee, H. M. 1984, ApJ, 285, 89
Du, F., Bergin, E. A., Hogerheijde, M., et al. 2017, ApJ, 842, 98
Dullemond, C. P., & Dominik, C. 2004, A&A, 417, 159
Fedoseev, G., Ioppolo, S., & Linnartz, H. 2015, MNRAS, 446, 449
Garrod, R. T., Wakelam, V., & Herbst, E. 2007, A&A, 467, 1103
Harju, J., Daniel, F., Sipilä, O., et al. 2017, A&A, 600, A61
Hartquist, T. W., & Williams, D. A. 1990, MNRAS, 247, 343
Hasegawa, T. I., & Herbst, E. 1993, MNRAS, 261, 83
Hidaka, H., Watanabe, M., Kouchi, A., & Watanabe, N. 2011, Physical Chemistry Chemical Physics (Incorporating Faraday Transactions), 13, 15798
Hiraoka, K., Yamashita, A., Yachi, Y., et al. 1995, ApJ, 443, 363
Huang, J., Öberg, K. I., Qi, C., et al. 2017, ApJ, 835, 231
Kama, M., Folsom, C. P., & Pinilla, P. 2015, A&A, 582, L10
Le Gal, R., Hily-Blant, P., Faure, A., et al. 2014, A&A, 562, A83
Mathews, G. S., Klaassen, P. D., Juhász, A., et al. 2013, A&A, 557, A132
Mumma, M. J., & Charnley, S. B. 2011, ARA&A, 49, 471
Öberg, K. I., Boogert, A. C. A., Pontoppidan, K. M., et al. 2011, ApJ, 740, 109
Öberg, K. I., Qi, C., Wilner, D. J., & Hogerheijde, M. R. 2012, ApJ, 749, 162
Pillai, T., Kauffmann, J., Wyrowski, F., et al. 2011, A&A, 530, A118
Pontoppidan, K. M., Salyk, C., Bergin, E. A., et al. 2014, Protostars and Planets VI, 363
Prasad, S. S., & Tarafdar, S. P. 1983, ApJ, 267, 603
Roueff, E., Lis, D. C., van der Tak, F. F. S., Gerin, M., & Goldsmith, P. F. 2005, A&A, 438, 585
Roueff, E., Loison, J. C., & Hickson, K. M. 2015, A&A, 576, A99

Salinas, V. N., Hogerheijde, M. R., Mathews, G. S., et al. 2017, ArXiv e-prints, arXiv:1707.06475
Salinas, V. N., Hogerheijde, M. R., Bergin, E. A., et al. 2016, A&A, 591, A122
Schöier, F. L., van der Tak, F. F. S., van Dishoeck, E. F., & Black, J. H. 2005, A&A, 432, 369
Schwarz, K. R., & Bergin, E. A. 2014, ApJ, 797, 113
Sipilä, O., Harju, J., Caselli, P., & Schlemmer, S. 2015, A&A, 581, A122
Treviño-Morales, S. P., Pilleri, P., Fuente, A., et al. 2014, A&A, 569, A19
van Dishoeck, E. F., Thi, W.-F., & van Zadelhoff, G.-J. 2003, A&A, 400, L1
van Dishoeck, E. F., Kristensen, L. E., Benz, A. O., et al. 2011, PASP, 123, 138
Walsh, C., Nomura, H., & van Dishoeck, E. 2015, A&A, 582, A88
Zhang, K., Bergin, E. A., Blake, G. A., et al. 2016, ApJ, 818, L16